(Received 29 July 2025, Accepted 15 October 2025, Scheduled 28 October 2025)

Demagnetization Fault Diagnosis of Permanent Magnet Synchronous Motor Based on IEWT-SSA-ELM

Dehai Chen[1,2], Jinpeng Xu[1,*], Zhijun Li[1], and Hao Gong[1]

[1] School of Electrical Engineering and Automation, Jiangxi University of Science and Technology, Ganzhou 341000, Jiangxi, China
[2] Ganjiang Innovation Academy, Chinese Academy of Sciences, Ganzhou 341000, Jiangxi, China

ABSTRACT: Aiming at the problems of weak distinctiveness and low diagnostic accuracy of permanent magnet synchronous motor (PMSM) demagnetization faults, a local demagnetization fault diagnosis method for PMSM based on Improved Empirical Wavelet Transform (IEWT) combined with Sparrow Search Algorithm (SSA) optimized Extreme Learning Machine (ELM) is proposed. Taking the radial leakage magnetic signal on a motor surface as the research object, the leakage magnetic experimental data under 15 different demagnetization states are extracted. To solve the problem of unreasonable spectrum segmentation in the EWT method, an adaptive decomposition with improved frequency band division is performed according to the special spectrum trend of PMSM leakage magnetic signals. Then, the normalized energy values of each intrinsic mode function (IMF) are calculated to form the corresponding feature vectors, which are input into the ELM model optimized by the SSA algorithm for demagnetization state identification. Experimental results show that the method based on IEWT-SSA-ELM has a significant improvement in fault identification effect compared with the unimproved and unoptimized methods.

1. INTRODUCTION

Permanent magnet synchronous motors (PMSMs) have become indispensable driving equipment in modern industry due to their significant advantages such as simple structure, high efficiency, high power density, and easy control [1]. They have broad application prospects in industrial automation production, new energy vehicles, wind power generation, aerospace, and other fields [2–4]. Permanent magnets are important components in PMSM, and their magnetic field distribution directly affects the output performance of PMSM [5]. However, during actual operation, permanent magnets are affected by multiple factors such as high temperature, armature reaction, and chemical corrosion, which easily lead to irreversible attenuation of magnetic properties [6, 7]. This demagnetization phenomenon will reduce the performance of the motor, destroy the system stability, and thus cause potential safety hazards [8, 9]. Therefore, the detection of permanent magnet demagnetization state is of great significance for the safe and reliable operation of PMSM.

At present, scholars' research on PMSM demagnetization fault diagnosis tends to consider two aspects: fault feature signal extraction and artificial intelligence algorithm prediction.

In terms of signal extraction, spectrum analysis is usually performed on the radial air gap magnetic density, stator current, back electromotive force, vibration signal, zero-sequence voltage, and leakage magnetic signal of PMSMs to realize the diagnosis of demagnetization faults. Ref. [10] effectively diagnoses the uniform demagnetization fault of permanent magnets by obtaining the motor's radial air gap magnetic density and stator current signals and comparing the average magnetic density of healthy and faulty motors under the same stator current. Ref. [11] locates and evaluates the degree of demagnetized permanent magnets by installing detection coils in stator slots and extracting back electromotive force residuals, but this method has the problem that detection coils are difficult to install, which limits its practical application. Ref. [12] realizes the diagnosis of partial permanent magnet demagnetization faults by extracting fault feature signals from motor vibration noise. Ref. [13] uses the zero-sequence voltage component of the stator phase voltage as a fault indicator parameter to realize online diagnosis of permanent magnet demagnetization faults. Ref. [14] obtains the motor's radial leakage magnetic signal and combines empirical wavelet transform (EWT) and Hilbert-Huang transform (HHT) for time-frequency analysis to effectively determine the demagnetization fault of PMSM magnets and fault location. This method is a non-contact fault diagnosis method with the advantage of not requiring motor disassembly, thus saving costs, but it is only applicable to the demagnetization of one or multiple pairs of magnetic poles.

In the field of artificial intelligence, researchers usually use machine learning methods such as back propagation (BP) neural network, least squares support vector machine (LSSVM), probabilistic neural network (PNN), and extreme learning machine (ELM) for fault regression prediction or classification prediction. Ref. [15] uses an improved genetic algorithm to optimize the BP neural network to realize the diagnosis of 8 typical faults of permanent magnet synchronous motors in electric vehicles. Ref. [16] uses the fault diagnosis model established by LSSVM to identify different demagnetization degrees of permanent magnets. This model has high diagnostic accuracy for

* Corresponding author: Jinpeng Xu (2639754138@qq.com).

permanent magnets with high demagnetization degrees, but its accuracy for weak faults needs to be improved. Ref. [17] proposes a rolling bearing fault diagnosis method based on variational mode decomposition (VMD) and LSSVM, which effectively classifies 7 types of bearing faults with an identification accuracy of 95.6%. Ref. [18] uses the PNN algorithm to realize the accurate classification of 15 demagnetization faults of permanent magnet synchronous linear motors. Compared with the traditional BP neural network, this method has higher fault identification accuracy but involves more detection steps and a relatively complex process. Ref. [19] proposes a fault diagnosis method for wind turbine gearboxes based on SSA-optimized ELM. Compared with traditional particle swarm optimization (PSO) and grey wolf optimizer (GWO), SSA has higher diagnostic accuracy after optimizing ELM.

To sum up, the current PMSM demagnetization fault diagnosis still has problems such as low distinguishability and complex detection procedures. To simplify the local demagnetization fault diagnosis process and improve accuracy, this paper uses the radial leakage magnetic signal that can directly reflect magnetic properties as the demagnetization feature signal. The normalized energy values of each intrinsic mode function (IMF) after improved EWT decomposition are calculated to form corresponding feature vectors, which are input into the SSA optimized ELM model for permanent magnet demagnetization state identification.

2. PMSM MODELING AND DEMAGNETIZATION FAULT SIGNAL EXTRACTION

2.1. PMSM Parameters and Finite Element Model

The finite element model has the advantages of simplicity, intuitiveness, strong simulation ability, and high simulation accuracy, and is widely used in engineering control. In this paper, Maxwell 2D is used to establish a two-dimensional finite element model of the motor. Table 1 shows the specific structural parameters of a conventional surface-mounted permanent magnet synchronous motor, and Fig. 1 shows the finite element model established according to the parameters.

TABLE 1. Parameters of the permanent magnet synchronous motor.

Parameter/Unit	Value
Stator outer diameter/mm	205
Stator inner diameter/mm	127
Rotor outer diameter/mm	125.6
Rated speed/r·min^{-1}	1500
Number of poles	8
Number of stator slots	48
Permanent magnet thickness/mm	5
Permanent magnet material	N35SH
Materials of stator and rotor	DW315_50
Number of turns	20
Remanence of permanent magnet/T	1.1519
Stator and rotor core length/mm	98

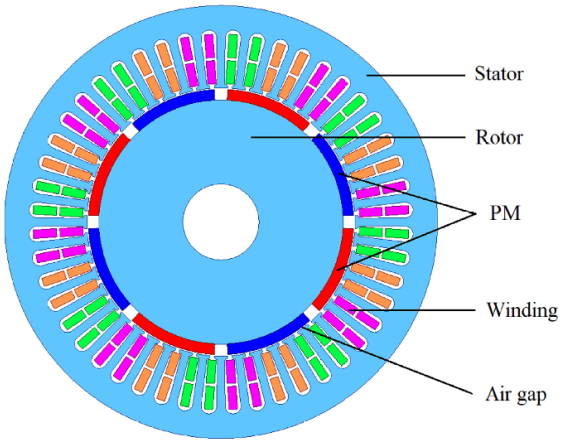

FIGURE 1. PMSM model.

2.2. Analysis of PMSM Demagnetization Fault Types

The rotor of the PMSM studied in this paper has 8 permanent magnets evenly distributed, and each permanent magnet may undergo different degrees of demagnetization, resulting in various types of uneven demagnetization of PMSM [20]. Due to the symmetry of the PMSM structure, therefore, analyzing the demagnetization fault status and severity of permanent magnets within half a cycle has reference significance for the demagnetization fault diagnosis of the entire motor. As shown in Fig. 2, half a cycle corresponds to two N-pole permanent magnets and two S-pole permanent magnets. These 4 permanent magnets are numbered 1, 2, 3, and 4, respectively, and several typical demagnetization faults are preset: permanent magnet 1 with 20% demagnetization, permanent magnet 2 with 30% demagnetization, permanent magnet 3 with 50% demagnetization, and permanent magnet 4 with 60% demagnetization [14, 18]. By arbitrarily combining them, there are a total of 15 combinations of permanent magnet demagnetization fault types, as shown in Table 2.

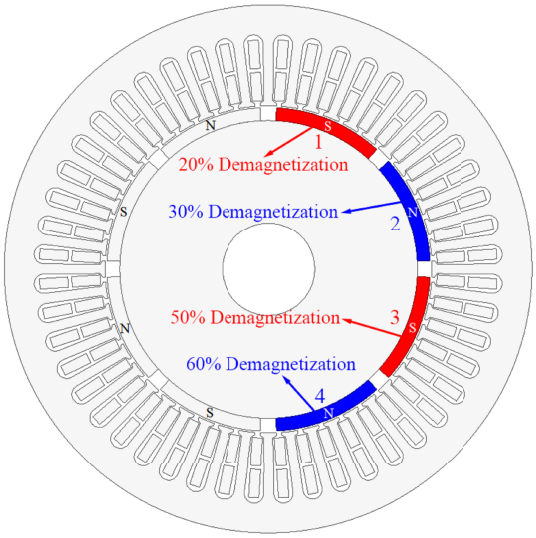

FIGURE 2. Preset typical demagnetization faults of the PMSM model.

TABLE 2. PMSM demagnetization fault types.

Fault type	Number of magnets	Magnetic steel combination
1	1	1
2	1	2
3	1	3
4	1	4
5	2	1-2
6	2	1-3
7	2	1-4
8	2	2-3
9	2	2-4
10	2	3-4
11	3	1-2-3
12	3	1-2-4
13	3	1-3-4
14	3	2-3-4
15	4	1-2-3-4

2.3. Extraction and Analysis of Radial Leakage Magnetic Signals

When a demagnetization fault occurs, the remanence Br and coercivity Hc of the permanent magnet will decrease accordingly. Therefore, different degrees of demagnetization can be simulated by changing these two parameters [21]. A finite element model is established according to the preset fault types, and simulation calculations are performed to obtain the leakage magnetic density distribution on the surface of the healthy motor and demagnetized motor, as shown in Fig. 3.

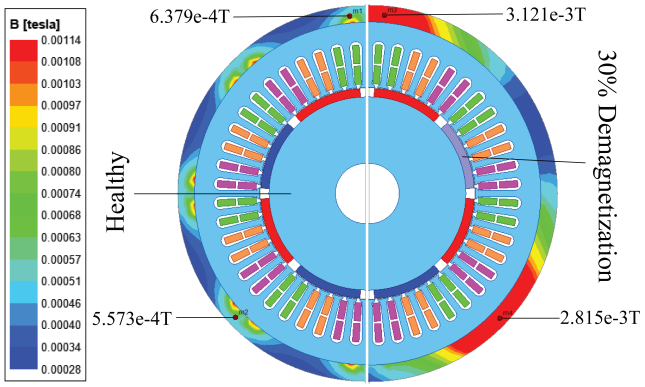

FIGURE 3. Distribution of leakage magnetic density on the motor surface.

It can be seen from Fig. 3 that the distributions of surface leakage magnetic density in the demagnetized motor and healthy motor are significantly different. Compared with traditional back electromotive force and air gap magnetic density signals, the leakage magnetic signal can not only directly reflect the health status of permanent magnets but also be easy to extract without disassembling the motor. Therefore, this paper selects radial leakage magnetic flux as the fault characteristic signal. To further study the characteristics of leakage magnetic signals, the normal state and 5 types of demagnetization faults are analyzed. The leakage magnetic signal waveforms when the motor rotates for one cycle are shown in Fig. 4, and the harmonic characteristics of these signals obtained by fast Fourier transform (FFT) are shown in Fig. 5.

It can be seen from Fig. 5 that the PMSM in the healthy state only has odd spatial harmonics such as $k = 1$, 3, and 5, while the demagnetized motor has non-odd fault harmonics in addition to odd spatial harmonics. Since the harmonics of the leakage magnetic signal change irregularly with the demagnetization type, the spectrum diagram alone can only determine whether the motor has a demagnetization fault but cannot accurately determine the demagnetization type. Therefore, further analysis is needed to enhance fault distinguishability.

3. DEMAGNETIZATION FAULT FEATURE EXTRACTION BASED ON IMPROVED EWT

3.1. EWT Algorithm

The EWT algorithm was proposed by Gilles in 2013 [22]. It overcomes the problems that wavelet transform requires predefined basis functions, and empirical mode decomposition (EMD) has mode mixing. The EWT algorithm divides the signal's Fourier spectrum into continuous intervals, filters by establishing a wavelet filter bank in each interval, and finally decomposes the signal into different frequency components [23]. Fig. 6 shows the frequency band division of the Fourier axis by EWT, with ω_n as the boundary of spectrum division, dividing it into N continuous segments.

The division result can be expressed as:

$$\Delta_n = [\omega_{n-1}, \omega_n], \quad n = 1, 2, ..., N \tag{1}$$

The support interval of the entire Fourier axis is:

$$\sum_{n=1}^{N} \Delta_n = [0, \pi] \tag{2}$$

The boundaries are determined by finding the maxima in the spectrum. The found maxima are sorted in descending order. Assuming that the angular frequencies corresponding to the first N maxima are Ω_n $(n{=}1, \ldots, N)$, the frequency band division boundaries of EWT are:

$$\omega_n = \frac{\Omega_n + \Omega_{n+1}}{2} \tag{3}$$

After dividing the Fourier spectrum into several frequency bands, empirical wavelet functions and empirical scaling functions are constructed using the idea of Meyer wavelets:

$$\hat{\psi}_n(\omega) = \begin{cases} 1, \text{ if } \omega_n + \tau_n \le |\omega| \le \omega_{n+1} - \tau_{n+1} \\ \cos\left[\frac{\pi}{2}\beta\left(\frac{1}{2\tau_{n+1}}\left(|\omega| - \omega_{n+1} + \tau_{n+1}\right)\right)\right], \\ \text{if } \omega_{n+1} - \tau_{n+1} \le |\omega| \le \omega_{n+1} + \tau_{n+1} \\ \sin\left[\frac{\pi}{2}\beta\left(\frac{1}{2\tau_n}\left(|\omega| - \omega_n + \tau_n\right)\right)\right], \\ \text{if } \omega_n - \tau_n \le |\omega| \le \omega_n + \tau_n \\ 0, \text{ others} \end{cases} \tag{4}$$

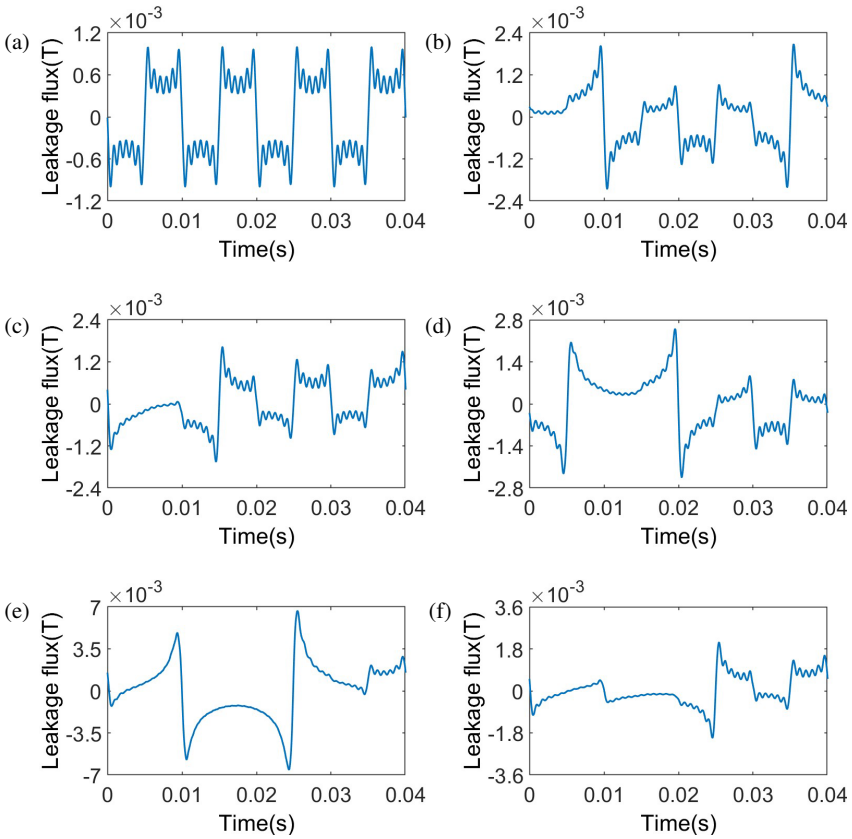

FIGURE 4. Leakage magnetic waveforms of 6 states. (a) Noemal. (b) Fault type 1. (c) Fault type 5. (d) Fault type 8. (e) Fault type 12. (f) Fault type 15.

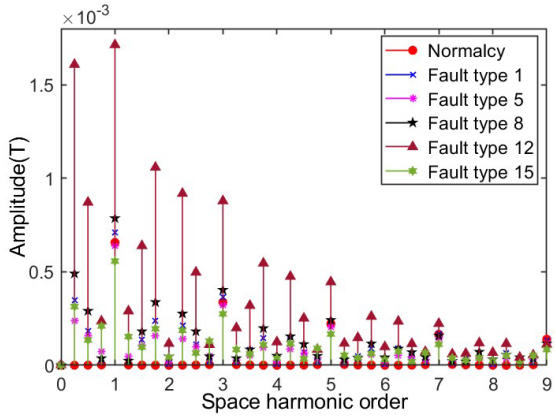

FIGURE 5. Harmonic orders of leakage magnetic signals in 6 states.

$$\hat{\varphi}_n(\omega) = \begin{cases} 1, \text{ if } |\omega| \le \omega_n - \tau_n \\ \cos\left[\frac{\pi}{2}\beta\left(\frac{1}{2\tau_n}\left(|\omega| - \omega_n + \tau_n\right)\right)\right], \\ \text{if } \omega_n - \tau_n \le |\omega| \le \omega_n + \tau_n \\ 0, \text{ others} \end{cases} \tag{5}$$

where:

$$\beta(x) = x^4\left(35 - 84x + 70x^2 - 20x^3\right) \tag{6}$$

$$\begin{cases} \tau_n = \gamma\omega_n \\ \gamma < \min_n\left(\frac{\omega_{n+1}-\omega_n}{\omega_{n+1}+\omega_n}\right) \end{cases} \tag{7}$$

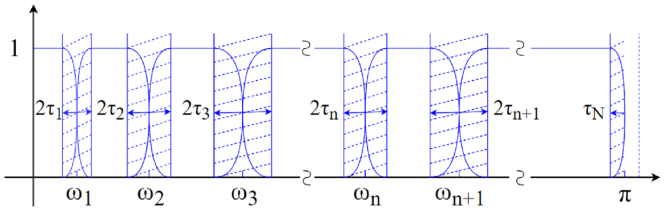

FIGURE 6. Frequency band division of Fourier spectrum.

For a signal $x(t)$, after EWT transformation, the approximation coefficient W_{fa} and detail coefficient W_{fd} can be obtained, which can be expressed as:

$$\begin{aligned} W_{fa}(0,t) &= \langle x(t), \varphi_1(t)\rangle = \int x(\tau)\overline{\varphi_1(\tau - t)}d\tau \\ &= F^{-1}(\widehat{x}(\omega)\overline{\widehat{\varphi}_1(\omega)}) \end{aligned} \tag{8}$$

$$\begin{aligned} W_{fd}(n,t) &= \langle x(t), \psi_n(t)\rangle = \int x(\tau)\overline{\psi_n(\tau - t)}d\tau \\ &= F^{-1}(\widehat{x}(\omega)\overline{\widehat{\psi}_n(\omega)}) \end{aligned} \tag{9}$$

where F^{-1} is the inverse Fourier transform, $^-$ the complex conjugate, and $\widehat{\ }$ the Fourier transform. The original signal $x(t)$ can be reconstructed as:

$$x(t) = W_{fa}(0,t)^*\varphi_1(t) + \sum_{n=1}^{N} W_{fd}(n,t)^*\psi_n(t)$$

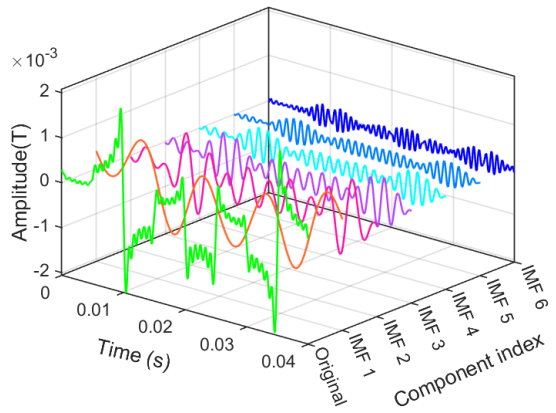

FIGURE 7. Time domain diagram of EWT decomposition.

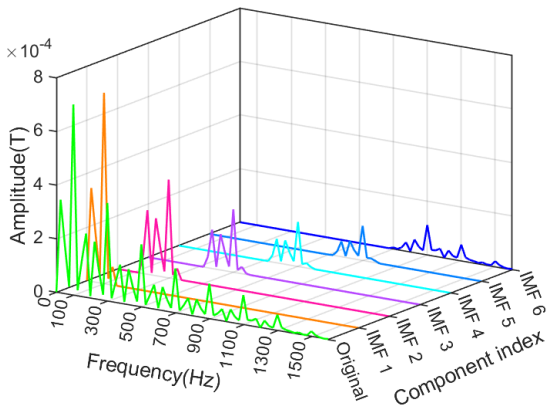

FIGURE 8. Spectrum diagram of EWT decomposition.

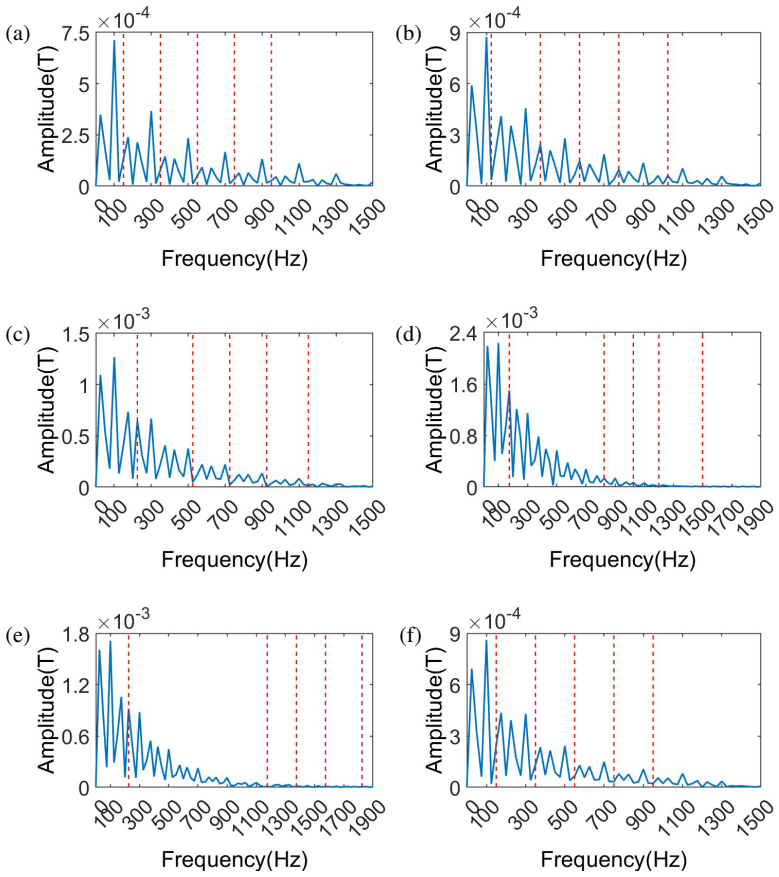

FIGURE 9. Frequency band division of leakage magnetic signals by EWT. (a) Fault type 1. (b) Fault type 2. (c) Fault type 6. (d) Fault type 7. (e) Fault type 12. (f) Fault type 13.

$$= F^{-1}\left[\widehat{W}_{fa}(0,\omega)^{*}\widehat{\varphi}_1(\omega) + \sum_{n=1}^{N}\widehat{W}_{fd}(n,\omega)^{*}\widehat{\psi}_n(\omega)\right] \quad (10)$$

where "*" denotes the convolution operation.

According to the principle of empirical wavelet transform, the leakage magnetic signal of fault type 1 is decomposed by EWT, and the decomposition results are shown in Fig. 7. To better analyze each IMF, FFT is performed on each component to obtain Fig. 8.

Figure 9 shows the frequency band division results of EWT for leakage magnetic signals of 6 demagnetization fault types. Combining Fig. 7 to Fig. 9, it can be seen that when the EWT algorithm is used to decompose the leakage magnetic signal, each IMF component is concentrated near its center frequency, and no mode mixing occurs. However, for leakage magnetic signals of different demagnetization fault types, the segmentation positions of their Fourier spectra vary greatly, which will affect subsequent fault feature extraction. Therefore, the EWT

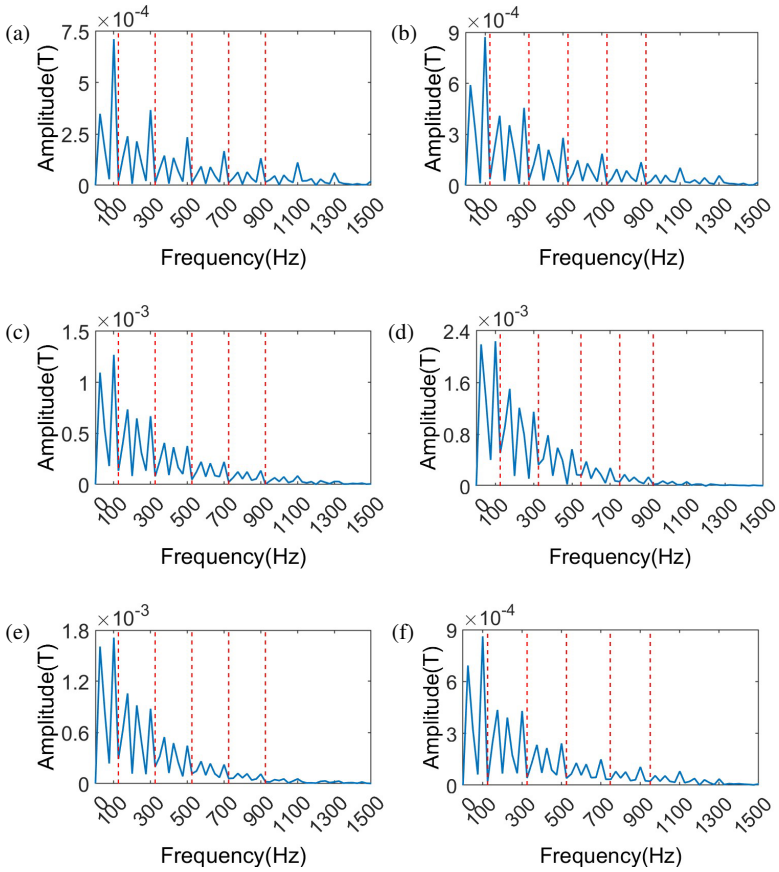

FIGURE 10. Frequency band division of leakage magnetic signals by IEWT. (a) Fault type 1. (b) Fault type 2. (c) Fault type 6. (d) Fault type 7. (e) Fault type 12. (f) Fault type 13.

algorithm needs to be improved to adapt to the decomposition of leakage magnetic signals.

3.2. EWT Decomposition with Improved Frequency Band Division

To solve the problem of unreasonable frequency band division in the EWT algorithm, adaptive decomposition with improved frequency band division is performed according to the special spectrum trend of PMSM leakage magnetic signals. The main difference from the original EWT decomposition algorithm is that the improved EWT determines the spectrum division positions based on both maxima points and odd fundamental frequencies. The PMSM studied in this paper has a rotational speed of 1500 r/min and a pole pair number of 4, so the fundamental frequency of the leakage magnetic signal is $f = 4 \times 1500/60 = 100$ Hz. First, the local maxima on the original signal spectrum are found and sorted in descending order. Then, only the maxima corresponding to all odd fundamental frequencies are retained. Finally, the first minimum to the right of these maxima is taken as the spectrum segmentation boundary. The flowchart of the improved EWT algorithm is shown in Fig. 13(a). Fig. 10 shows the frequency band division results of the improved EWT algorithm for leakage magnetic signals. This division method can better decompose the demagnetization fault features into different intrinsic mode functions.

3.3. Demagnetization Fault Feature Extraction and Sample Library Establishment Based on Improved EWT Algorithm

The leakage magnetic signals extracted in finite element simulations are from an ideal simulated environment without any noise, while signals measured in reality are usually accompanied by interference from useless information, and these interferences are random. Therefore, to simulate the feature signals extracted in practice as much as possible, random noise with a signal-to-noise ratio above 10 dB is added to the leakage magnetic signals. For each fault type, 100 different signal-to-noise ratios of noise are added, resulting in 100 samples for each fault type. For 15 fault types, there are a total of $15 \times 100 = 1500$ samples.

The obtained sample signals are decomposed by IEWT into 6 intrinsic mode functions. As shown in Fig. 11, it presents the energy proportion of each component after IEWT decomposition is performed on a set of signals of Fault type 1 and Fault type 15, respectively. Analysis shows that the first 5 IMF components account for more than 96% of the total energy, and the 6th IMF component is typically dominated by noise. Thus, the first 5 components are used for fault feature extraction. Assuming that the first 5 IMF components after decomposition are $x_i(t)$, $(i = 1, 2, ..., 5)$, their respective energies can be calculated as:

$$E_i = \sum_{j=1}^{n} x_i^2(t_j) \tag{11}$$

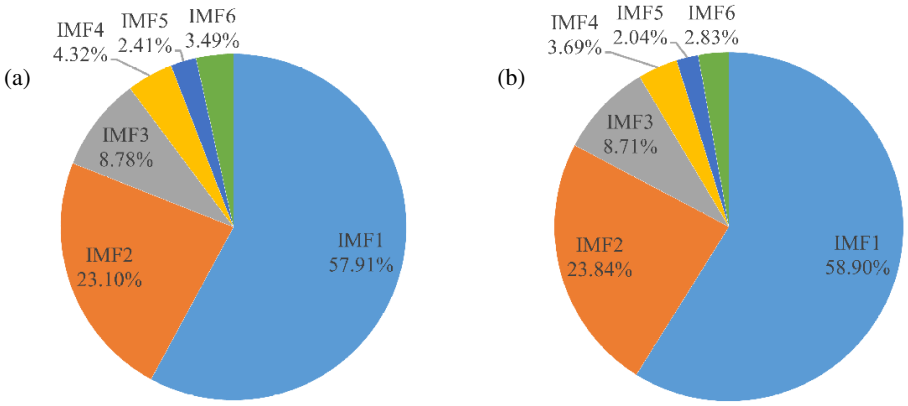

FIGURE 11. Energy distribution among components after IEWT decomposition. (a) Fault type 1. (b) Fault type 15.

where n is the number of signal points contained in each component, and the total energy of the signal is:

$$E = \sum_{i=1}^{5} E_i \tag{12}$$

Finally, the obtained energies are normalized to get a demagnetization feature vector:

$$X = \left[E_1/E, E_2/E, ..., E_5/E\right] \tag{13}$$

A total of 1500 sets of data samples are obtained through calculation, and some sample datasets are shown in Table 3.

4. SSA-ELM MODEL

4.1. Principle of SSA

The Sparrow Search Algorithm is a new swarm intelligence optimization algorithm proposed in 2020, inspired by the group cooperation behavior of sparrows during foraging and predator avoidance [24]. By simulating the division of labor mechanism of sparrow groups, the algorithm effectively balances global search and local optimization capabilities. The specific process is as follows:

Assume the population composed of n sparrows is:

$$X = \begin{bmatrix} x_1^1 & x_1^2 & \cdots & x_1^d \\ x_2^1 & x_2^2 & \cdots & x_2^d \\ \vdots & \vdots & \vdots & \vdots \\ x_n^1 & x_n^2 & \cdots & x_n^d \end{bmatrix} \tag{14}$$

where d is the dimension of the optimization variable, and the fitness function of the population is expressed as:

$$F_x = \begin{bmatrix} f\left(\left[x_1^1 & x_1^2 & \cdots & x_1^d\right]\right) \\ f\left(\left[x_2^1 & x_2^2 & \cdots & x_2^d\right]\right) \\ \vdots \\ f\left(\left[x_n^1 & x_n^2 & \cdots & x_n^d\right]\right) \end{bmatrix} \tag{15}$$

Discoverers are responsible for exploring safe areas, i.e., high-quality solution areas, and their position update formula is:

$$X_{i,j}^{t+1} = \begin{cases} X_{i,j}^t \cdot \exp\left(\frac{-i}{\alpha \cdot iter_{\max}}\right), & R_2 < ST \\ X_{i,j}^t + Q \cdot L, & R_2 \geq ST \end{cases} \tag{16}$$

where t is the current iteration number; $j = 1, 2 \cdots d$; $X_{i,j}^t$ represents the position of the ith sparrow in the jth dimension in the tth generation; $\alpha \in (0, 1]$ is a random number; Q is a random number following a standard normal distribution; L is a $1 \times d$ matrix; R_2 and ST are the early warning threshold and safety threshold, respectively. Followers move closer to discoverers, and their position update formula is:

$$x_{i,j}^{t+1} = \begin{cases} Q \cdot \exp\left(\frac{X_w^t - X_{i,j}^t}{i^2}\right), & i > n/2 \\ X_P^{t+1} + |X_{i,j}^t - X_P^{t+1}| \cdot A^+ \cdot L, & \text{otherwise} \end{cases} \tag{17}$$

where X_p is the optimal position of discoverers; A is a $1 \times d$ matrix with elements 1 or -1; X_w is the current global worst position. When some sparrow individuals are at the edge of the population, they are at a higher risk of predation due to exposure and will quickly move to the center of the population. At the same time, individuals in the center, sensing the threat, will actively move closer to other individuals to reduce their predation probability. These individuals are called vigilantes, and their position update can be expressed as:

$$X_{i,j}^{t+1} = \begin{cases} X_b^t + \beta \cdot |X_{i,j}^t - X_b^t|, & f_i > f_b \\ X_{i,j}^t + K \cdot \left(\frac{X_{i,j}^t - X_w^t}{(f_i - f_w) + \gamma}\right), & f_i = f_b \end{cases} \tag{18}$$

where X_b is the current global best position; β is a random number following a normal distribution; $K \in [-1, 1]$ is a random number; f_i is the current global best fitness value; f_b is the current global best fitness value; f_w is the current global worst fitness value; γ is a minimum constant to avoid a zero denominator.

TABLE 3. Partial fault feature vector datasets.

Fault type	Sample number	Feature vector				
		X_1	X_2	X_3	X_4	X_5
1	1	0.590	0.236	0.101	0.044	0.029
	2	0.583	0.244	0.092	0.051	0.030
	3	0.599	0.240	0.096	0.042	0.024
2	1	0.570	0.264	0.102	0.044	0.019
	2	0.567	0.274	0.092	0.046	0.022
	3	0.576	0.271	0.094	0.041	0.019
6	1	0.552	0.307	0.102	0.030	0.010
	2	0.549	0.303	0.098	0.034	0.016
	3	0.557	0.294	0.101	0.034	0.014
7	1	0.574	0.313	0.083	0.023	0.007
	2	0.559	0.332	0.083	0.020	0.006
	3	0.567	0.337	0.078	0.014	0.004
12	1	0.572	0.299	0.095	0.029	0.006
	2	0.562	0.324	0.084	0.024	0.006
	3	0.564	0.329	0.079	0.023	0.005
13	1	0.589	0.289	0.081	0.028	0.013
	2	0.583	0.275	0.093	0.031	0.017
	3	0.590	0.276	0.092	0.030	0.013

4.2. SSA Optimization of ELM

The Extreme Learning Machine is a randomized single-layer feedforward neural network learning algorithm proposed by Professor Huang et al. in 2006 [25]. Compared with other traditional machine learning algorithms, ELM has the advantages of good generalization performance, fast learning speed, and simple implementation. It can effectively shorten the learning time during training and is widely used in signal processing and fault detection fields. The network model of ELM is shown in Fig. 12, where $x_1 \sim x_n$ are input neuron nodes; ω_{11}~ω_{ni} are input weights; $g(x)$ is the activation function; b_1~b_i are thresholds of hidden layer nodes; $\beta_{11} \sim \beta_{ni}$ are weights between the hidden layer and the output layer; y_1~y_n are the outputs of the model.

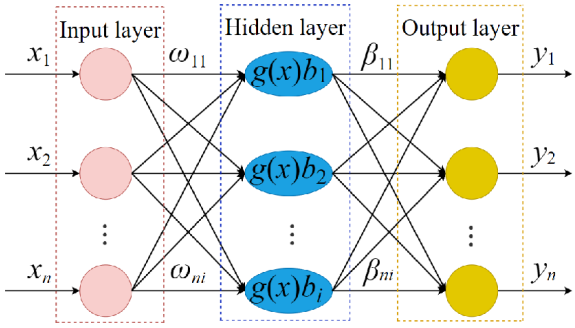

FIGURE 12. ELM network model.

Since the input weights ω and thresholds b of hidden layer neurons in ELM are randomly generated, it will affect the accuracy and stability of the classification model to a certain extent [26]. Therefore, this paper uses the Sparrow Search Algorithm to optimize ELM, replacing the originally randomly generated weights and thresholds with the optimal solution found by SSA and building an SSA-ELM fault classification model to improve its recognition rate. The flowchart of SSA optimizing ELM is shown in Fig. 13(c), and the specific process [19] is:

(1) Parameter initialization, including setting parameters such as population size, maximum number of iterations, early warning value, proportion of discoverers, and proportion of vigilantes;

(2) Population classification and fitness evaluation, divide population individuals into discoverers and followers, calculate fitness values, sort them, and select the current optimal and worst values;

(3) Update the positions of discoverers using formula (16);

(4) Update the positions of followers using formula (17);

(5) Randomly select vigilantes, update their positions using formula (18), and obtain the current optimal value;

(6) Compare the current iteration optimal solution with the historical optimal solution and retain the better one;

(7) Determine whether the maximum number of iterations is reached. If yes, output the optimal parameters; otherwise, return to step 2.

5. CLASSIFICATION AND IDENTIFICATION OF PMSM DEMAGNETIZATION FAULTS BASED ON IEWT-SSA-ELM

In this paper, the improved EWT algorithm is used to extract fault features from the extracted PMSM leakage magnetic signals, obtaining a series of demagnetization feature vectors, which are input into the SSA-ELM model for demagnetization

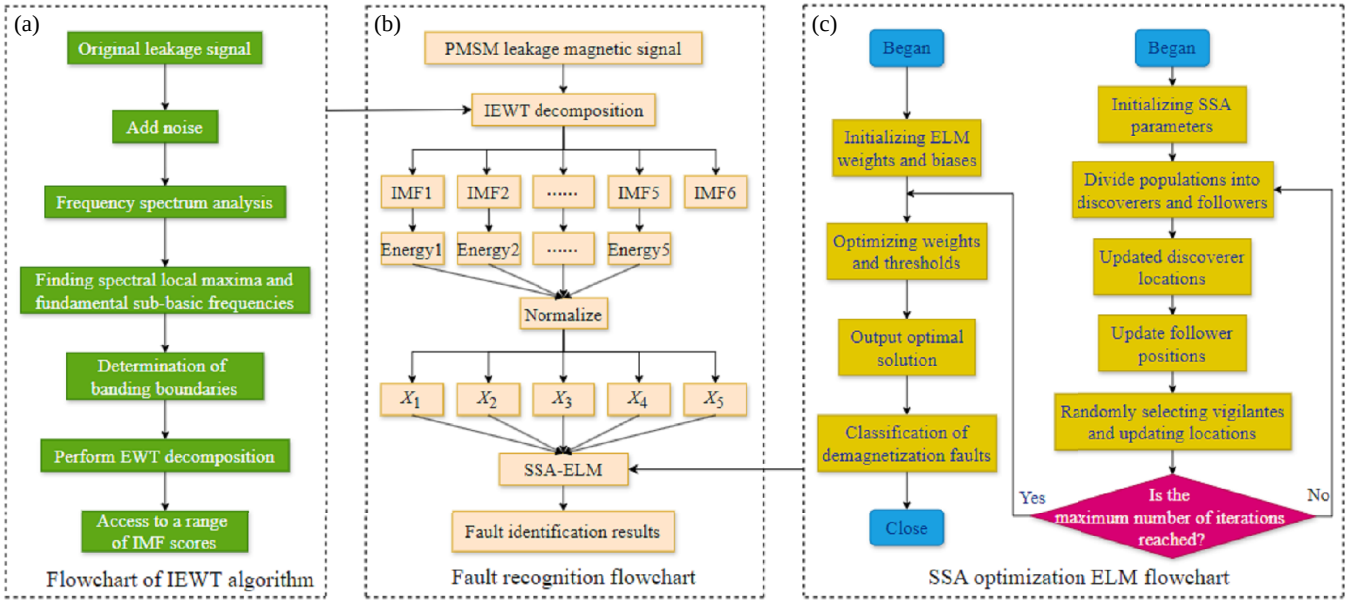

FIGURE 13. Overall flowchart of fault diagnosis.

fault diagnosis. It mainly includes two parts: classification of 15 demagnetization fault types and evaluation of the severity of permanent magnet demagnetization. The diagnosis flow is shown in Fig. 13(b), and the specific process is:

(1) Signal collection: extract the surface leakage magnetic signal of PMSM within one cycle at 5 mm from the stator surface, and considering both "sampling accuracy" and "timeliness", the number of sampling points is set to 1000;

(2) Data preprocessing: add random noise to the leakage magnetic signal, then perform improved EWT decomposition to obtain 6 IMF components;

(3) Fault feature extraction: calculate the energy values of the first 5 IMFs and normalize them to obtain a series of demagnetization feature vector datasets;

(4) Determine the diagnostic model structure: use the SSA algorithm to find the optimal solution of weights and thresholds and input them into the ELM model;

(5) Divide the dataset into training samples and test samples in an 8 : 2 ratio, establish the SSA-ELM fault diagnosis model, and perform PMSM demagnetization fault diagnosis.

5.1. Identification and Classification of PMSM Demagnetization Fault Types

A sample library of 15 PMSM demagnetization fault types in Table 2 is established. Stratified sampling is performed on the obtained 1500 samples: 80 groups of each type are randomly selected as training samples and the remaining 20 groups as test samples. A total of $80 \times 15 = 1200$ samples are used to train the SSA-ELM model, and 300 samples are used to test it. Through repeated experiments, the relevant parameters of SSA were set as follows: the sparrow population size was 30; the maximum number of iterations was 100; the proportion of discoverers was 40%; the proportion of sentinels was 20%; the early warning threshold was 0.7. The final testing results are

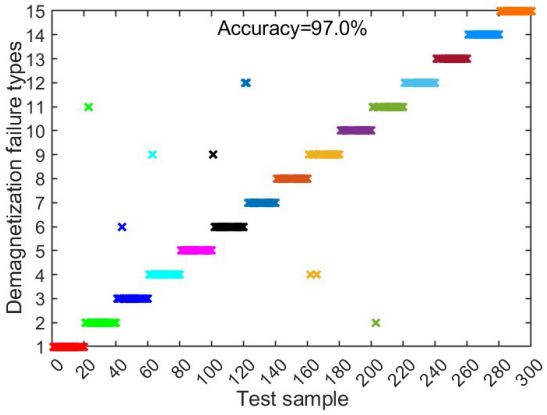

FIGURE 14. Recognition results of demagnetization fault types.

presented in Fig. 14. It can be seen that 9 samples are incorrectly tested in the IEWT-SSA-ELM model among 300 samples, with a demagnetization fault type recognition accuracy of 97%.

5.2. Identification and Classification of PMSM Demagnetization Severity

By identifying the PMSM demagnetization fault types, the location of demagnetized permanent magnets can be determined, and then the demagnetization severity of permanent magnets needs to be evaluated. Due to space limitations, this paper only classifies the demagnetization severity of permanent magnet 1. Demagnetization faults are divided into 4 categories according to severity: healthy, mild, moderate, and severe. Demagnetization from 0% to 5% is considered healthy, 6% to 20% as mild, 21% to 50% as moderate, and 51% to 100% as severe. Leakage magnetic signals of 4 demagnetization severity types are collected; fault features are extracted using the signal processing method described in this paper; then classification and identi-

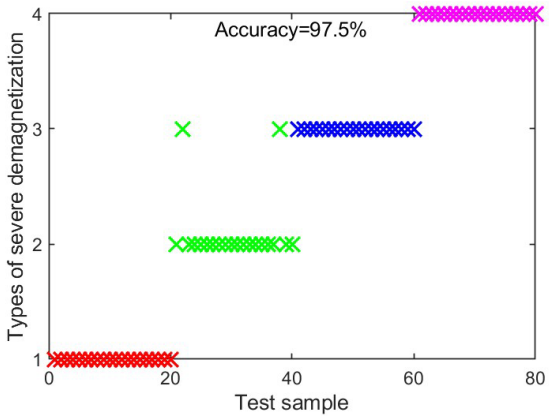

FIGURE 15. Recognition results of demagnetization severity.

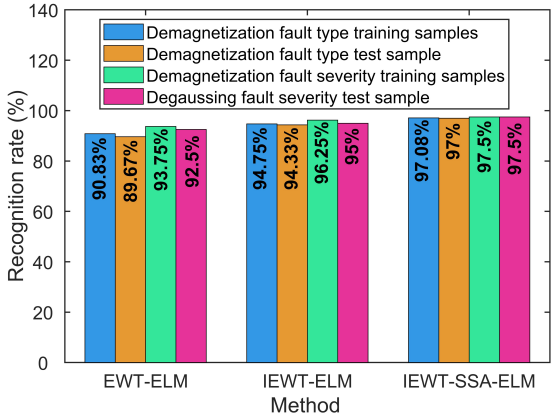

FIGURE 16. Comparison of classification results of three methods.

fication are performed. A fault sample library of 4 different demagnetization severities is established in the above manner, with 100 samples for each severity, totaling 400 samples. 320 groups are taken as training samples and the other 80 groups as test samples. The recognition results are shown in Fig. 15.

5.3. Comparative Experiment Verification

To clearly demonstrate the advantages of the method described in this paper, the IEWT-SSA-ELM method is compared with the EWT-ELM and IEWT-ELM methods. The comparison results of recognition rates of the three methods are shown in Fig. 16. It can be seen that the method based on IEWT-SSA-ELM has higher classification accuracy than the EWT-ELM and IEWT-ELM methods and can be used for the diagnosis of PMSM local demagnetization faults.

6. CONCLUSION

To classify and identify different demagnetization types and degrees of PMSM magnets and improve fault diagnosis accuracy, a local demagnetization fault diagnosis method for PMSM based on IEWT combined with SSA-optimized ELM is proposed. A two-dimensional finite element model of the motor is built, and radial leakage magnetic signals are used as the motor's demagnetization feature signals to establish a fault sample library of 15 different demagnetization types. Aiming at the problem of unreasonable spectrum segmentation in the EWT algorithm, adaptive decomposition with improved frequency band division is performed by analyzing the spectral characteristics of leakage magnetic signals. Experimental results show that the IEWT algorithm can avoid unreasonable spectrum segmentation and more effectively extract demagnetization fault features compared with the original algorithm; the IEWT-SSA-ELM classification model has higher recognition rates in both demagnetization type and severity classification than the EWT-ELM and IEWT-ELM classification models, providing a new and simpler and effective method for PMSM local demagnetization fault diagnosis.

ACKNOWLEDGEMENT

National Class A Major Research Project of China (Project Number: E210E001010).

REFERENCES

[1] Li, Y.-J., Z.-L. Zhang, M.-H. Li, H.-F. Wei, and Y. Zhang, "Fault diagnosis of inter-turn short circuit of permanent magnet synchronous motor based on deep learning," *Electric Machines and Control*, Vol. 24, No. 9, 173–180, 2020.

[2] Gritli, Y., M. Mengoni, G. Rizzoli, C. Rossi, A. Tani, and D. Casadei, "Rotor magnet demagnetisation diagnosis in asymmetrical six-phase surface-mounted AC PMSM drives," *IET Electric Power Applications*, Vol. 14, No. 10, 1747–1755, 2020.

[3] Li, Y., H. Li, H. Geng, X. Gong, and F. Yang, "Measurement and analysis of hysteresis loss of Nd-Fe-B permanent magnet under superheated loss of magnetism," *Electric Power*, Vol. 53, No. 10, 50–57, 2020.

[4] Jung, J.-W., B.-H. Lee, K.-S. Kim, and S.-I. Kim, "Interior permanent magnet synchronous motor design for eddy current loss reduction in permanent magnets to prevent irreversible demagnetization," *Energies*, Vol. 13, No. 19, 5082, 2020.

[5] Xie, Y., W. Xin, W. Cai, *et al.*, "Electromagnetic performance and electromagnetic vibration noise analysis of different rotor topologies of interior permanent magnet synchronous motor," *Electric Machines and Control*, Vol. 27, No. 1, 110–119, 2023.

[6] Zhang, Y., G. Liu, and Q. Chen, "Discrimination of interturn short-circuit and local demagnetization in permanent magnet synchronous motor based on current fluctuation characteristics," *Transactions of China Electrotechnical Society*, Vol. 37, No. 7, 1634–1643, 2022.

[7] Chen, H., C. X. Gao, X. C. Sang, *et al.*, "Toroidal yoke search-coil-based method for locating fault in PMSM with local demagnetization fault," *Electric Machines and Control*, Vol. 27, No. 4, 97, 2023.

[8] Zhang, X., K. Yan, and W. Zhang, "Hybrid double vector model predictive control for open-winding permanent magnet synchronous motor with common DC bus," *Transactions of China Electrotechnical Society*, Vol. 36, No. 1, 96–106, 2021.

[9] Zhao, K. H., A. J. Leng, J. He, *et al.*, "Reconstruction of demagnetization fault of six-phase permanent magnet synchronous motor based on super-twisting sliding-mode observer," *Journal of Electronic Measurement and Instrumentation*, Vol. 34, No. 10, 123–131, 2020.

[10] Ding, S. C., W. He, J. Hang, *et al.*, "Uniform demagnetization fault diagnosis for PMSM based on radial air-gap flux density and stator current," *Proceedings of the CSEE*, Vol. 44, No. 1, 332–340, 2024.

[11] Gao, C. X., B. K. Li, H. Chen, *et al.*, "Local demagnetization fault diagnosis of permanent magnet synchronous motor based on half-period back EMF residual," *Electric Machines and Control*, Vol. 27, No. 7, 183–194, 2023.

[12] Torregrossa, D., A. Khoobroo, and B. Fahimi, "Prediction of acoustic noise and torque pulsation in PM synchronous machines with static eccentricity and partial demagnetization using field reconstruction method," *IEEE Transactions on Industrial Electronics*, Vol. 59, No. 2, 934–944, 2012.

[13] Urresty, J.-C., J.-R. Riba, M. Delgado, and L. Romeral, "Detection of demagnetization faults in surface-mounted permanent magnet synchronous motors by means of the zero-sequence voltage component," *IEEE Transactions on Energy Conversion*, Vol. 27, No. 1, 42–51, 2012.

[14] Zhou, S. W., Y. Q. Yu, H. X. Gao, Q. P. Chen, W. Wang, and P. Liu, "Diagnosis of local demagnetization fault in PMSM based on EWT-HHT and radial leakage field," *Journal of Magnetic Materials and Devices*, Vol. 53, No. 5, 97–104, 2022.

[15] Qiao, W. D., "Research of fault diagnosis model for electric vehicle permanent magnet synchronous motor on BP neural network," *Journal of Shijiazhuang University*, Vol. 26, No. 6, 50–55, 2024.

[16] Li, Z., Y. Cao, and X. Xing, "Demagnetization model design of PMSM based on maxwell 2D and simplorer," *Fire Control & Command Control*, Vol. 41, No. 7, 135–139, 2016.

[17] Xie, F., Y. Jiang, Q. Xiao, Y. Fu, E. Wang, and Y. Liu, "VMD-LSSVM fault identification method for rolling bearings," *Mechanical Science and Technology for Aerospace Engineering*, Vol. 42, No. 9, 1482–1489, 2023.

[18] Zhang, D., J. W. Zhao, F. Dong, J. C. Song, S. K. Dou, H. Wang, and F. Xie, "Partial demagnetization fault diagnosis research of permanent magnet synchronous motors based on the PNN algorithm," *Proceedings of the CSEE*, Vol. 39, No. 1, 296–306, 2019.

[19] Liu, X.-Y., Z.-M. Zhang, L.-G. Zhao, F.-W. Meng, and Y. Zhang, "Fault diagnosis of wind turbine gearbox based on CEEMDAN sample entropy and SSA-ELM," *Modular Machine Tool & Automatic Manufacturing Technique*, Vol. 63, No. 9, 126–130, 2022 (in Chinese).

[20] Liu, S., J. C. Song, S. L. Lu, *et al.*, "Demagnetization fault diagnosis research of DPPMSLM based on gray texture feature extraction and CS-SNN," *Proceedings of the CSEE*, Vol. 43, No. 16, 6464–6473, 2023.

[21] Zhang, M. and Y. Yu, "Permanent magnet synchronous motor demagnetization fault diagnosis based on leakage radial magnetic density," in *Journal of Physics: Conference Series*, Vol. 2708, No. 1, 012008, Nanning, China, 2024.

[22] Gilles, J., "Empirical wavelet transform," *IEEE Transactions on Signal Processing*, Vol. 61, No. 16, 3999–4010, 2013.

[23] Wang, H., "Research on rolling bearing fault diagnosis method based on improved empirical wavelet transform," Ph.D. dissertation, Yanshan University, Hebei, China, 2020.

[24] Chen, X., X. Zheng, S. Wang, and D. Liu, "SSA-ELM-based optical cable fault pattern recognition method," *Laser Journal*, Vol. 43, No. 5, 49–53, 2022.

[25] Huang, G.-B., Q.-Y. Zhu, and C.-K. Siew, "Extreme learning machine: Theory and applications," *Neurocomputing*, Vol. 70, No. 1–3, 489–501, 2006.

[26] Li, M.-Y., Q. Zhou, and Z.-Q. Yu, "Gearbox fault diagnosis based on kernel principal component analysis and optimized ELM," *Modular Machine Tool & Automatic Manufacturing Technique*, No. 4, 87–90, 2021 (in Chinese).